



# Structure and mixing of a meandering turbulent chemical plume: turbulent mixing and eddy diffusivity

David L. Young<sup>1,2</sup> · Donald R. Webster<sup>1</sup> · Ann I. Larsson<sup>1,3</sup>

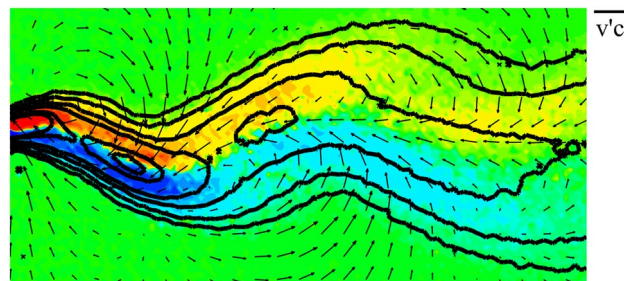
Received: 8 July 2021 / Revised: 8 November 2021 / Accepted: 14 November 2021

© The Author(s), under exclusive licence to Springer-Verlag GmbH Germany, part of Springer Nature 2021

## Abstract

Turbulent mixing in a meandering non-buoyant chemical plume is far less understood than in a straight plume—partially due to difficulty separating the plume meander from the turbulent fluctuations. This study presents high-resolution measurements of the covariance of the turbulent fluctuations of velocity and concentration, i.e., the turbulent flux, in a phase-locked meandering plume, acquired by simultaneous particle tracking velocimetry and laser-induced fluorescence measurements. Analysis of the data reveals that the spatial distribution of the turbulent quantities is governed by the large-scale alternating-sign vortices that induce the plume meander. Further, the spatial variation of turbulent flux agrees well with the spatial variation of the phase-averaged concentration gradient. As a result, the eddy diffusivity framework effectively models the turbulent flux. As expected from turbulent mixing theory, the eddy diffusivity coefficient plateaus at a constant value once the plume width reaches the size of the largest eddies. However, when the plume width is less than the size of the largest eddies, the eddy diffusivity coefficient scales with the plume width to the  $n=1$  power. Analysis based on the measurements of the growth rate of the plume width yields a consistent prediction for the variation of the eddy diffusivity coefficient in the near field.

## Graphical abstract



## 1 Introduction

Turbulent chemical plumes often have a meandering characteristic that is defined as large-scale displacement of the plume centerline. Based on the velocity and concentration fields reported in Young et al. (2021), the induced motion by the large-scale vortices explains the spatial distribution of the concentration filaments and further helps to explain the turbulent mixing and concentration dilution. However, a number of questions remain beyond the phase-averaged velocity and concentration fields, especially questions about the turbulence quantities and how they relate to the

✉ Donald R. Webster  
dwebster@ce.gatech.edu

David L. Young  
david.l.young@usace.army.mil

<sup>1</sup> School of Civil and Environmental Engineering, Georgia Institute of Technology, 790 Atlantic Drive, Atlanta, GA 30332, USA

<sup>2</sup> Present Address: US Army Corps of Engineers, 1261 Duck Road, Kitty Hawk, NC 27949, USA

<sup>3</sup> Present Address: Department of Marine Sciences, Tjärnö Marine Laboratory, University of Gothenburg, 45296 Strömstad, Sweden

large-scale alternating-sign vortices that induce the plume meander.

One clear observation is that the Gifford (1959) model is insufficient to explain the phase-averaged concentration field. Gifford (1959) assumes turbulent diffusion (or dispersion) processes are separated from the scales that induce the meander. The turbulent diffusion model explains the lateral spread of the phase-averaged concentration field, and the symmetric, transverse profiles of the phase-averaged concentration (same as for the straight plume) are simply displaced laterally from the main axis due to the plume-scale meander. This conceptualization of the plume structure has been followed by many subsequent studies including Csanady (1973), Sawford and Stapountzis (1986), Hanna (1986), and Talluru et al. (2018). But, the measurements reported by Young et al. (2021) show that transverse symmetry of the phase-averaged concentration is not present in a meandering plume. Further, advection of scalar filaments by the alternating-sign vortices leads to a non-monotonically decreasing phase-averaged concentration along the plume centerline.

Despite the lack of symmetry of the transverse phase-averaged concentration profiles, there is some suggestion that eddy diffusivity concepts may successfully model the turbulent mixing of the concentration field. For instance, the transverse profiles of the phase-averaged concentration field match a Gaussian profile in segmented manner (i.e., the left and right sides of the profile have different half-widths, but each matches a Gaussian profile shape), and a Gaussian profile shape is consistent with an eddy diffusivity process. Further, iso-contours of the phase-averaged concentration are nearly perpendicular to transects that are perpendicular to the local plume centerline (see Fig. 8 in Young et al. 2021). These characteristics suggest eddy diffusivity concepts may effectively model the turbulent flux down the phase-averaged concentration gradient. The planar velocity and concentration measurements in this study facilitate testing the effectiveness of the eddy diffusivity model. The following subsection reviews turbulent mixing and the eddy diffusivity model in greater detail.

## 1.1 Turbulent mixing

Mixing of scalar quantities, such as mass and heat, occurs rapidly in a turbulent flow field due to the fact that turbulent diffusion processes are substantially more efficient at mixing scalars than molecular diffusion (Roberts and Webster 2002). The wide range of eddy sizes in a turbulent flow plays a key role in the efficiency of turbulent mixing. For a patch of scalar of a given size, turbulent eddies *smaller* than the patch continuously stretch and distort it (e.g., Batchelor 1952; Roberts and Webster 2002). As a result, extremely large local concentration gradients occur, which are quickly smoothed out by molecular diffusion—the flux

due to molecular diffusion is proportional to the concentration gradient. Thus, the patch increases in size and the scalar is diluted. In contrast, eddies *larger* than the patch merely advect the patch and do not contribute to mixing (e.g., Batchelor 1952; Roberts and Webster 2002).

The evolution equation for the time-averaged scalar concentration field in a turbulent flow is:

$$\frac{\partial \bar{c}}{\partial t} + \bar{u}_j \frac{\partial \bar{c}}{\partial x_j} = D \frac{\partial^2 \bar{c}}{\partial x_j^2} - \frac{\partial}{\partial x_j} \overline{u'_j c'} \quad (1)$$

where a Reynolds decomposition of both the concentration and the velocity is employed (i.e.,  $c = \bar{c} + c'$  and  $u = \bar{u} + u'$ ) to separate the mean (denoted with an overbar) and fluctuating (denoted with a prime) components. The two terms on the right-hand-side represent the molecular diffusion ( $D \frac{\partial^2 \bar{c}}{\partial x_j^2}$ ,

where  $D$  is the molecular diffusivity) and the flux of scalar due to the turbulent velocity fluctuations ( $\frac{\partial}{\partial x_j} \overline{u'_j c'}$ ), respectively. Turbulent flux is typically much more effective at mixing scalars than molecular diffusion, i.e.,  $\frac{\partial}{\partial x_j} \overline{u'_j c'} \gg D \frac{\partial^2 \bar{c}}{\partial x_j^2}$ .

Consequently, the molecular diffusivity is typically neglected (Roberts and Webster 2002) and the turbulent advection–diffusion equation is approximated as:

$$\frac{\partial \bar{c}}{\partial t} + u \frac{\partial \bar{c}}{\partial x} + v \frac{\partial \bar{c}}{\partial y} + w \frac{\partial \bar{c}}{\partial z} = - \frac{\partial}{\partial x} \overline{u' c'} - \frac{\partial}{\partial y} \overline{v' c'} - \frac{\partial}{\partial z} \overline{w' c'} \quad (2)$$

Note that the overbar denoting mean value is typically dropped at this stage and it is understood that  $c = \bar{c}$ ,  $u = \bar{u}$ , etc. Unfortunately, the  $\overline{u'_j c'}$  terms are unknown and this equation is not closed. To mathematically model the equation, the covariance of the velocity and concentration fluctuations are frequently modeled as a Fickian diffusion process (i.e., “mass transport is proportional to the mean concentration gradient,” Roberts and Webster 2002), only with a much larger diffusion coefficient, called the eddy, or turbulent, diffusivity coefficient,  $K_i$ , e.g.:

$$\overline{v' c'} = -K_y \frac{\partial \bar{c}}{\partial y} \quad (3)$$

The eddy diffusivity coefficient varies based upon the flow type and the location within the flow, and thus it is typically specified using experimental data (Roberts and Webster 2002). In one recent example, the eddy diffusivity approach has been applied to slender chemical plumes in a uniformly sheared flow (Vanderwel and Tavoularis 2014).

A natural question is how to estimate the eddy diffusivity coefficient using easily measured properties of the flow. Richardson (1926) and Batchelor (1952) proposed relationships for the eddy diffusivity coefficient for patches of size less than the Lagrangian length scale,  $L_L$ , which is the spatial distance for which the particle motion in the scalar patch is

assumed to be well correlated. The size of the Lagrangian length scale is closely related to the size of the largest turbulent eddies, which dictate the length over which the flow is well correlated (Roberts and Webster 2002). The Richardson (1926) and Batchelor (1952) relationships follow from the assumptions of isotropic turbulence and that the characteristic patch size,  $L$ , is located within the inertial subrange of the turbulent power spectrum (see Batchelor 1952 and Okubo 1968). The existence of the inertial subrange is justified by the assumption of high Reynolds number flow such that the separation between the Kolmogorov microscale ( $\eta$ ) and the integral length scale ( $l$ ) is sufficiently large. Based on empirical analysis of atmospheric diffusion data, Richardson (1926) hypothesized that the eddy diffusivity coefficient  $K$  was proportional to  $L^{4/3}$ , whereas Batchelor (1952), using a more rigorous consideration of the joint PDF of two fluid particles and the Kolmogorov (1941) similarity hypothesis, concluded that  $K \sim (\sqrt{L^2})^{4/3}$ .

The similarities between the two formulations are obvious, and indeed the latter (Batchelor 1952) is often offered as proof of the former (Richardson 1926), e.g., in Fischer et al. (1979) and Roberts and Webster (2002). However, while both formulations predict the same growth rate of the time variance of the separation distance between two particles in a turbulent flow, they result in different shapes of the distance neighbor function—the function that describes the probability that a pair of particles have a given separation distance among all particles pairs in a scalar patch at a specific time. The analysis in Liao and Cowen (2010) indicates that the Richardson (1926) scaling better predicts the distance neighbor function for a plume in a turbulent boundary layer.

## 1.2 Aim of study

The applicability of the eddy diffusivity concept is explored in this study by examining turbulent mixing in the meandering plume presented in Young et al. (2021). Simultaneous laser-induced fluorescence (LIF) and particle tracking velocimetry (PTV) measurements of the phase-locked meandering plume structure facilitate measuring turbulence quantities, including the turbulent flux quantities. The phase-locked data provide a natural means to examine the mixing effects occurring at different scales, specifically the scale of the meandering motion induced by the large two-dimensional vortices and the smaller-scale three-dimensional turbulent diffusion (or dispersion). The separation of scales is consistent with previous conceptualizations by Gifford (1959), Fong and Stacey (2003), Jones et al. (2008), and others. The turbulence quantities and eddy diffusivity model will be discussed in the context of the phase-averaged velocity and concentration fields presented in Young et al.

(2021) as well as the large-scale alternating-sign vortices that induce the plume meander.

## 2 Materials and methods

Measurements consisted of simultaneous particle tracking-velocimetry (PTV) and laser-induced-fluorescence (LIF) measurements to quantify the velocity vector field and the concentration field, respectively, in a meandering turbulent plume. The experimental design is essentially the same as that described in Young et al. (2021). The primary difference is that the images used for the particle image velocimetry (PIV) measurements described in Young et al. (2021) are processed using PTV in this study. The advantage of PTV, compared to particle image velocimetry (PIV), is greater spatial resolution, which produces superior measurements of turbulence quantities (e.g., Webster et al. 2001; Cowen et al. 2001).

### 2.1 Experimental design

The experiment was performed in a 1.07 m wide by 24.4 m long rectangular cross section tilting flume. Uniform depth ( $H = 200 \pm 0.1$  mm) flow was created for at least 12 m upstream of the test section by adjusting the tailgate position and bed slope. Tracy and Lester (1961) and Rahman and Webster (2005) confirmed that a fully developed turbulent boundary layer is generated in the test section under these conditions. The sidewall of the flume in the vicinity of the test section is glass. A PVC plastic diverting plate suspended in the flume induced the plume meandering. The base of the plate was positioned less than 1 mm above the flume bed and the top of the plate extended above the free surface. The period of the plate oscillation ( $T$ ) was 9.5 s, and the amplitude of the transverse displacement of the downstream edge of the plate was 5.08 cm. The diverting plate was designed such that the flow characteristics in the wake were analogous to the wake downstream of a 10.1 cm circular cylinder for the same water depth and free-stream velocity ( $H = 200$  mm and  $U = 50$  mm/s, respectively). The resulting Strouhal number is  $St = 0.21$ . The advantage of a meandering plume generated by a periodically-oscillating plate is that it allowed the extraction of a trigger signal (via a mechanical trigger attached to the diverting plate apparatus) to collect data at specified phases in the plate motion.

The passive scalar (fluorescent dye) for the LIF measurements was released 400 mm downstream of the center of the diverting plate and 46 mm upstream of the test section. The dye was released iso-kinetically through a 4.2-mm-diameter nozzle, located 20 mm above the flume bed. The 1.2-cm-long nozzle fairing was streamlined to minimize the

flow disturbance (Webster et al. 2003; Rahman and Webster 2005).

## 2.2 Optics

Illumination for the LIF measurements was provided by a 10-W argon-ion laser (Coherent Innova 90, Coherent Inc., Santa Clara, CA) with a wavelength of 514 nm. The illumination for the PTV measurements was provided by a 4.6 W Krypton-ion laser (Coherent Innova Sabre, Coherent Inc., Santa Clara, CA) with a wavelength of 647.1 nm. The laser beams were swept in the streamwise direction 20 mm above the flume bed (the same height as the fluorescent dye release). The LIF and PTV images were captured with two side-by-side digital cameras (sCMOS pco.edge, PCO AG, Kelheim, Germany) operating in global shutter mode and mounted 1.5 m above the flume bed at the test section. The cameras captured 16-bit  $2560 \times 2160$  pixel images that span 1000 mm of the flume in the streamwise direction and 840 mm in the transverse direction. Calibration images for the PTV and LIF images were collected and processed in the DaVis software (LaVision GmbH, Göttingen, Germany) to yield a 3<sup>rd</sup>-order polynomial spatial distortion calibration function. The images from each camera were also aligned and indexed in this process. During the experiments and image calibration, a 19-mm-thick acrylic sheet was suspended just above the water surface (wetting the bottom surface of the sheet only) to prevent optical distortion from the free surface.

## 2.3 Timing system and laser scanning

The PTV and LIF images were acquired simultaneously for four phases ( $\varphi = 0^\circ$ ,  $\varphi = 90^\circ$ ,  $\varphi = 150^\circ$ , and  $\varphi = 240^\circ$ ) in the diverting plate motion. Phase  $\varphi = 0^\circ$  is defined as the maximum transverse displacement of the diverting plate position. For the LIF dataset, 6706 images were acquired for each phase, with a 9.5 s delay between successive images of a given phase. Similarly, for the PTV dataset, 6706 image pairs were acquired for each phase with the first and second frames of the image pair separated by 55 ms. The timing of the LIF-laser sweep was at the mid-time-point between the two PTV-laser sweeps.

## 2.4 Laser-induced fluorescence

The fluorescent dye used in the LIF measurements was Rhodamine 6G, which has peak light absorption near 530 nm (close to the wavelength of the Argon-ion laser) and peak emission near 560 nm (Arcoumanis et al. 1990). The plume source concentration was chosen to be 1 mg/L to make use of the full dynamic range of the LIF camera. The images from the LIF camera were captured using the Camware software (PCO AG, Kelheim, Germany) resulting in 16-bit images.

The images were imported into the DaVis software to calculate the concentration fields using the LIF analysis package. The LIF calibration function described in Young et al. (2021) was used to calculate the dye concentration from the emitted light intensity. The uncertainty in the instantaneous concentration measurement was estimated to be  $\pm 3\%$  based on several factors including the calibration procedure.

## 2.5 Particle tracking velocimetry and turbulent flux calculation

PTV requires successive images of the moving fluid seeded with tracer particles (as with PIV) in order to obtain velocity vector measurements in a fluid. PTV techniques attempt to match individual particles in successive frames rather than relying on an image cross-correlation (as with PIV) (e.g., Maas et al. 1993; Malik et al. 1993; Cowen and Monismith 1997). The local velocity is calculated as the displacement of the particle divided by the time between the two frames. This results in highly spatially resolved, but unevenly distributed, velocity vectors, as the velocity vectors are calculated only where particle matches are found rather than on a uniform grid. The PTV velocity vectors were obtained from the same set of images as the PIV measurements reported in Young et al. (2021). Figure 1 shows an example velocity field resulting from the PTV analysis, with the concentration field superimposed, at the same moment as the example PIV field shown in Young et al. (2021). The measurement uncertainty for the velocity vectors was estimated to be  $\pm 2\%$  based on the accuracy of the particle location estimates.

The velocity vector estimates from the PTV analysis were used to determine the turbulent flux terms (due to their greater spatial resolution than the PIV velocity

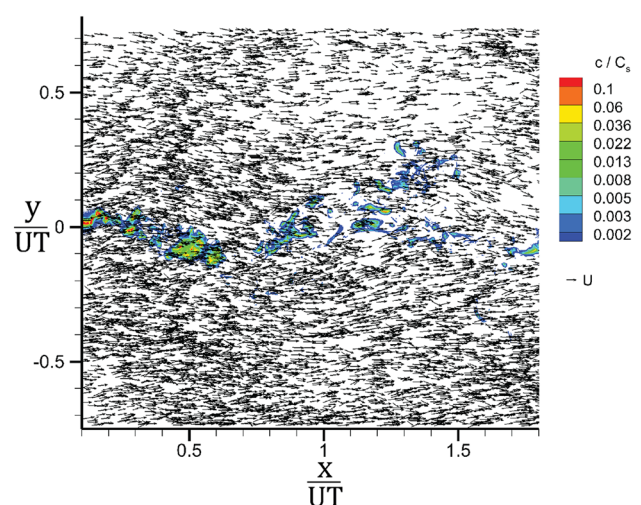


**Fig. 1** Example simultaneous velocity (PTV) and concentration fields (LIF) of the meandering plume for phase  $\varphi = 0^\circ$ . Note the concentration contours are logarithmically spaced



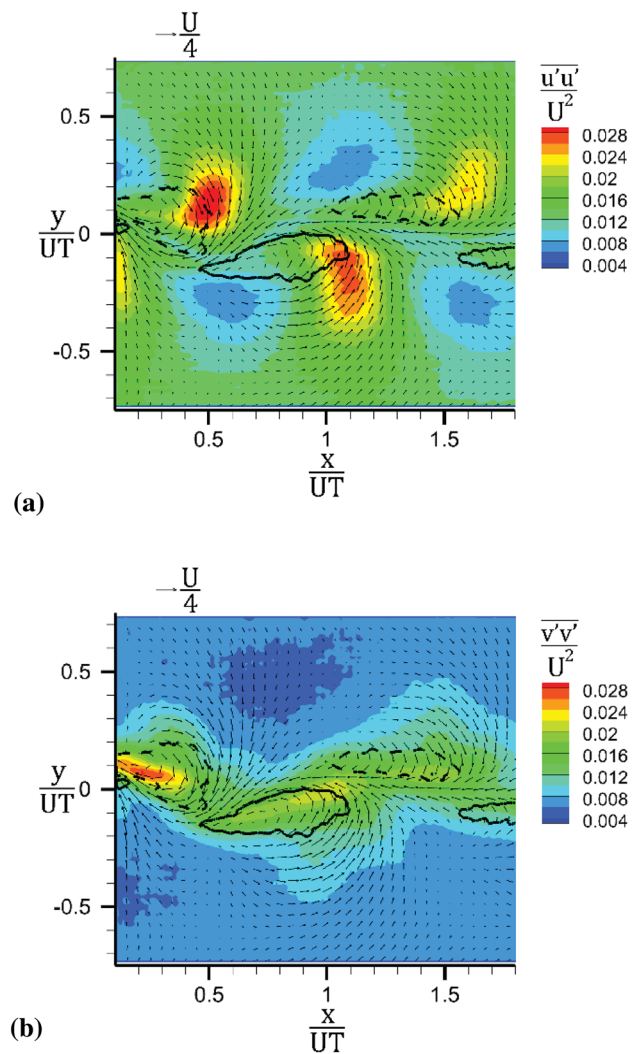
measurements). The PTV processing algorithm in DaVis yielded approximately 12,000 velocity vectors for each of the 6706 image-pairs. Prior to calculating the turbulent flux terms, the velocity vectors were filtered using an adaptive filtering algorithm to remove spurious vectors (Cowen and Monismith 1997; Webster et al. 2001). To perform the adaptive filtering, the camera viewing window was partitioned into  $16 \times 16$  pixel bins, and then the phase-average and standard deviation of the  $x$ - and  $y$ -components of velocity were calculated for each bin. Spurious vectors were identified as those in which either component of the velocity lay outside the range of the phase-averaged velocity component plus/minus a coefficient multiplied by the standard deviation of the velocity component for the bin. These vectors were identified and removed, and then the procedure was repeated until no vectors were identified for removal. For the first pass of the adaptive filtering algorithm, the standard deviation coefficient was 2, and for each subsequent pass it was 3. Approximately 2.5% of the PTV velocity vectors were removed via the adaptive filtering.

The turbulent flux terms ( $\overline{u'c'}$  and  $\overline{v'c'}$ ) were calculated by combining the LIF measurement of concentration with the PTV measurement of the velocity vector following the approach described by Webster et al. (2001). The value of the instantaneous concentration, with the phase-averaged concentration subtracted, was computed at the position of each PTV velocity vector to estimate  $c'$ . The phase-averaged velocity was estimated at the position of each PTV velocity vector by interpolating the phase-averaged velocity from the PIV results (Young et al. 2021). The phase-averaged velocity was subtracted from the instantaneous PTV velocity vector to estimate  $u'$  and  $v'$ . The field was partitioned into  $16 \times 16$  pixel bins, and  $\overline{u'c'}$  and  $\overline{v'c'}$  were calculated as the ensemble average of  $u'c'$  and  $v'c'$  for every PTV vector located in each bin over the duration of the experiment. The value was reported at the centroid of the bin. As a check of the validity of this procedure, the phase-averaged turbulent shear stress was also acquired from the PTV velocity fields using the same binning method. The resulting estimates of  $\overline{u'v'}$  using the phase-averaged velocity from the PTV measurements agreed well with those using the PIV phase-averaged velocity fields.

### 3 Results and discussion

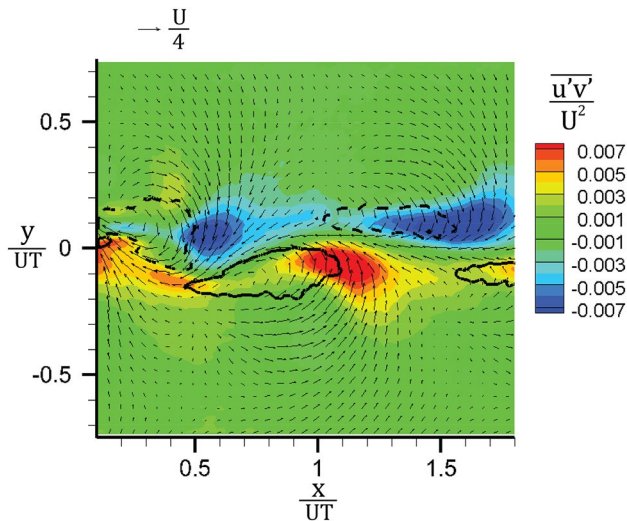
#### 3.1 Reynolds normal and shear stresses

Figure 2 shows Reynolds normal stresses for the meandering plume for phase  $\varphi = 0^\circ$ . The streamwise normal stress,  $\overline{u'u'}$ , is greatest toward the downstream edge of the large-scale alternating-sign vortices and is smallest near the upstream edge. The spatial extent of the vortices is visualized as the



**Fig. 2** Reynolds normal stresses (a) in the  $x$ -direction ( $\overline{u'u'}/U^2$ ) and (b) in the  $y$ -direction ( $\overline{v'v'}/U^2$ ) for the meandering plume for phase  $\varphi = 0^\circ$ . Vorticity contours corresponding to levels  $T\omega_z = -1.3$  and  $T\omega_z = 1.3$  are shown as dashed and solid black lines, respectively. The vectors indicate the phase-averaged velocity with the free-stream velocity ( $U$ ) subtracted. Every 4th velocity vector is plotted

iso-contours of vorticity levels  $T\omega = -1.3$  and  $T\omega = 1.3$  in Fig. 2 and subsequent figures. As described in Young et al. (2021), the vortex cores were also identified using the  $\lambda_2$ -criterion (Jeong and Hussain 1995); however, the iso-contours of vorticity are preferred since they identify the same region and are slightly smoother curves compared to the  $\lambda_2$  iso-contours. In the freestream region away from the vortex structure,  $\overline{u'u'}$  does not approach zero due to the presence of the turbulent boundary layer. The regions of greatest  $\overline{v'v'}$  are also co-located with the vortex structure, and unsurprisingly, the regions of smallest  $\overline{v'v'}$  are far from the plume in the free-stream where the phase-averaged velocity gradients are smallest. Figure 3 shows the spatial distribution of the



**Fig. 3** Reynolds shear stress ( $\overline{u'v'}/U^2$ ) for the meandering plume for phase  $\varphi=0^\circ$ . Vorticity contours corresponding to levels  $T\omega_z=-1.3$  and  $T\omega_z=1.3$  are shown as dashed and solid black lines, respectively. The vectors indicate the phase-averaged velocity with the free-stream velocity ( $U$ ) subtracted. Every 4th velocity vector is plotted

Reynolds shear stress ( $\overline{u'v'}$ ) for the meandering plume for phase  $\varphi=0^\circ$ . The regions of greatest Reynolds shear stress magnitude are located near the leading edge of the large-scale alternating-sign vortices, in roughly the same region of the peak regions of  $\overline{u'u'}$ . The Reynolds shear stress is negative in the vicinity of the leading edge of the clockwise-rotating vortices and positive in the vicinity of the leading edge of the counterclockwise-rotating vortices. Further, the Reynolds shear stress is near zero on the plume centerline and farther away from the plume in the free-stream.

The spatial distributions of Reynolds normal and shear stresses in Figs. 2 and 3 can be compared to those of other studies of periodic vortices shed from bluff bodies, such as rectangular (Lyn et al. 1995; Nakagawa et al. 1999; Saha et al. 2000) or circular (Huang et al. 1995; Kim et al. 2006) cylinders. As in this study, the normal stresses are largest within (or adjacent to) the cores of the large-scale alternating vortices (Lyn et al. 1995; Nakagawa et al. 1999; Saha et al. 2000). Further, the Reynolds shear stress magnitudes are largest on the leading edge of the large-scale alternating-sign vortices in Lyn et al. (1995), Huang et al. (1995), and Kim et al. (2006) and near zero along the hypothetical centerline between the vortices, similar to the distribution reported in this study. A difference of note is that the region of maximum observed Reynolds normal stresses, most notably  $\overline{u'u'}$ , in the current study is located toward the downstream edge of the vortices, as opposed to the vortex center as in Lyn et al. (1995). Similarly, the peaks in the Reynolds shear stress magnitudes are located slightly farther downstream

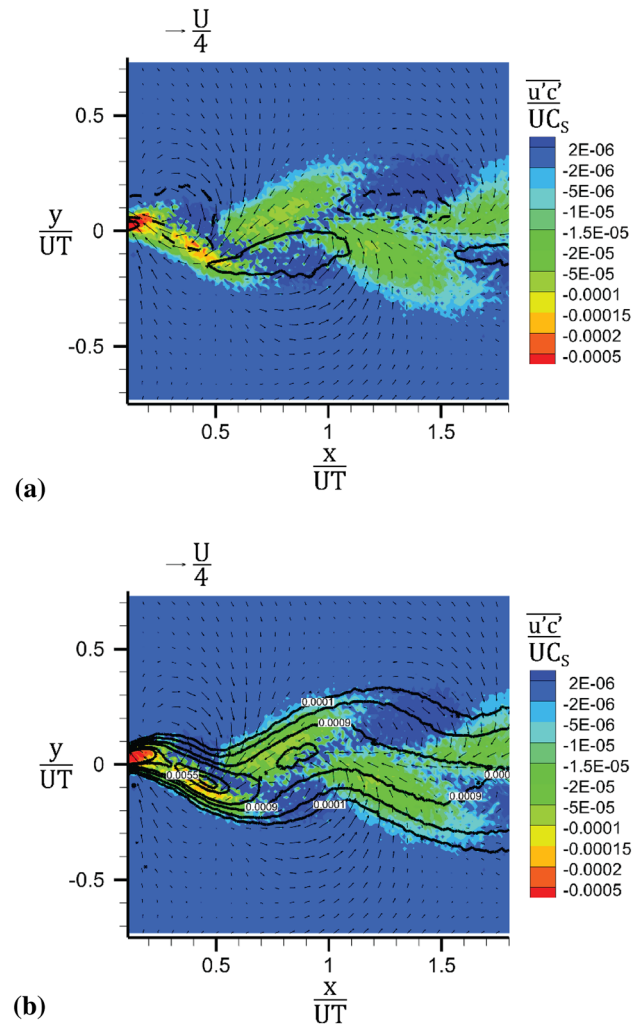


**Fig. 4** Turbulent flux in the  $x$ -direction ( $\overline{u'c'}/UC_s$ ) for the meandering plume for phase  $\varphi=0^\circ$ . (a) Vorticity iso-contours corresponding to levels  $T\omega_z=-1.3$  and  $T\omega_z=1.3$  are shown as dashed and solid black lines, respectively. (b) Phase-averaged concentration iso-contour lines are shown in black (note they are logarithmically spaced). The vectors indicate the phase-averaged velocity with the free-stream velocity ( $U$ ) subtracted. Every 5th velocity vector is plotted

of the vortex cores in the current study than observed in Lyn et al. (1995), Huang et al. (1995), and Kim et al. (2006). This is likely the result of the shape of the vortices being shed. In the previous studies, the vortices are close to circular in shape, whereas the vortices in the current study are more elliptical in shape with a noticeably greater influence on the velocity field at the downstream edges of the vortices.

### 3.2 Turbulent flux

Figures 4 and 5 show  $\overline{u'c'}$  and  $\overline{v'c'}$ , respectively, for the meandering plume for phase  $\varphi=0^\circ$ . As shown in Fig. 4, the largest magnitude of streamwise turbulent flux  $\overline{u'c'}$

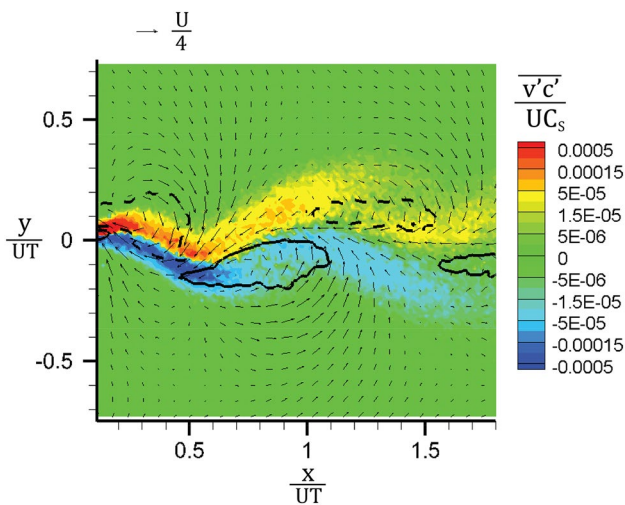


**Fig. 5** Turbulent flux in the  $y$ -direction ( $\overline{v'c'}/UC_s$ ) for the meandering plume for phase  $\varphi=0^\circ$ . Vorticity iso-contours corresponding to levels  $T\omega_z=-1.3$  and  $T\omega_z=1.3$  are shown as dashed and solid black lines, respectively. The vectors indicate the phase-averaged velocity with the free-stream velocity ( $U$ ) subtracted. Every 5th velocity vector is plotted

occurs immediately downstream of the large-scale alternating-sign vortices (roughly co-located with the peak regions of the Reynolds shear stress observed in Fig. 3), and  $\overline{u'c'}$  decreases in magnitude with downstream distance. The streamwise turbulent flux is negative throughout most of the field, although there are weak positive regions just downstream of the peak negative regions. As shown in Fig. 4b, the peak negative regions of  $\overline{u'c'}$  are located where the phase-averaged concentration gradient is positive in the streamwise direction. This explains why  $\overline{u'c'}$  is negative, as one would expect a negative correlation of streamwise velocity fluctuations and concentration fluctuations. The smaller magnitude observed in the positive  $\overline{u'c'}$  regions is partially explained by the milder streamwise gradient of the phase-averaged concentration field in these regions. There also may be a negative bias for  $\overline{u'c'}$  due to transport from the edges of the plume, as explained by Vanderwel and Tavoularis (2014) for a slender plume in a uniformly sheared flow. Figure 5 indicates that the locations of the largest magnitudes of  $\overline{v'c'}$  occur immediately to either side of the plume centerline. As with the distribution of Reynolds shear stress in Fig. 3,  $\overline{v'c'}$  changes sign across the plume centerline (albeit with negative  $\overline{v'c'}$  at negative values of  $y/UT$  and positive  $\overline{v'c'}$  at positive values of  $y/UT$  due to the difference in the transverse transport of the scalar versus transverse transport of the streamwise momentum). As with  $\overline{u'c'}$ ,

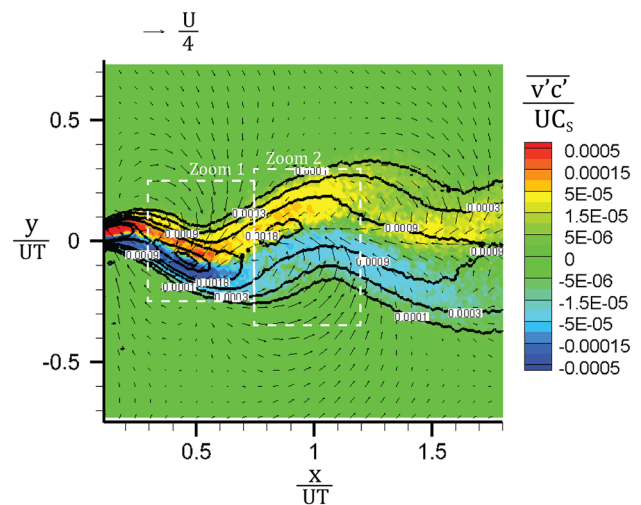


**Fig. 6** Turbulent flux in the  $y$ -direction ( $\overline{v'c'}/UC_s$ ) for the meandering plume for phase  $\varphi=0^\circ$ . Phase-averaged concentration iso-contour lines are shown in black (note they are logarithmically spaced). The vectors indicate the phase-averaged velocity with the free-stream velocity ( $U$ ) subtracted. Every 5th velocity vector is plotted. The white boxes define the zoom regions

the transverse turbulent flux  $\overline{v'c'}$  decreases in magnitude with downstream distance.

### 3.3 Estimating the eddy diffusivity coefficient

As described in Introduction, the turbulent flux is commonly modeled by assuming that it is equivalent to the mean concentration gradient multiplied by an eddy diffusivity coefficient, e.g.,  $\overline{v'c'} = -K_{\partial c/\partial y}$ , analogous to a Fickian diffusion process. To investigate the possibility of applying this model to the turbulent mixing in the meandering plume, Fig. 6 shows the spatial distribution of  $\overline{v'c'}$  along with the phase-averaged concentration iso-contour lines for the meandering plume for phase  $\varphi=0^\circ$ . The two sub-windows, “zoom 1” and “zoom 2,” outlined in white in Fig. 6 are re-plotted in Fig. 7a and b, respectively. The turbulent flux in the  $y$ -direction  $\overline{v'c'}$  is plotted in Fig. 7 rather than  $\overline{u'c'}$  because (1) the greatest concentration gradient is more closely aligned with the  $y$ -axis, and (2) one expects advective transport to dominate the turbulent flux of scalar in the  $x$ -direction. These figures strongly suggest that the turbulent flux for the meandering plume may be modeled as a function of the concentration gradient. The turbulent flux in the  $y$ -direction  $\overline{v'c'}$  is zero on the centerline, where the phase-averaged concentration is maximum and the concentration gradient in the  $y$ -direction is zero. Further, the phase-averaged concentration gradient in the  $y$ -direction changes sign across the plume, as does the sign of  $\overline{v'c'}$ . Finally, the magnitude of  $\overline{v'c'}$  appears to co-vary



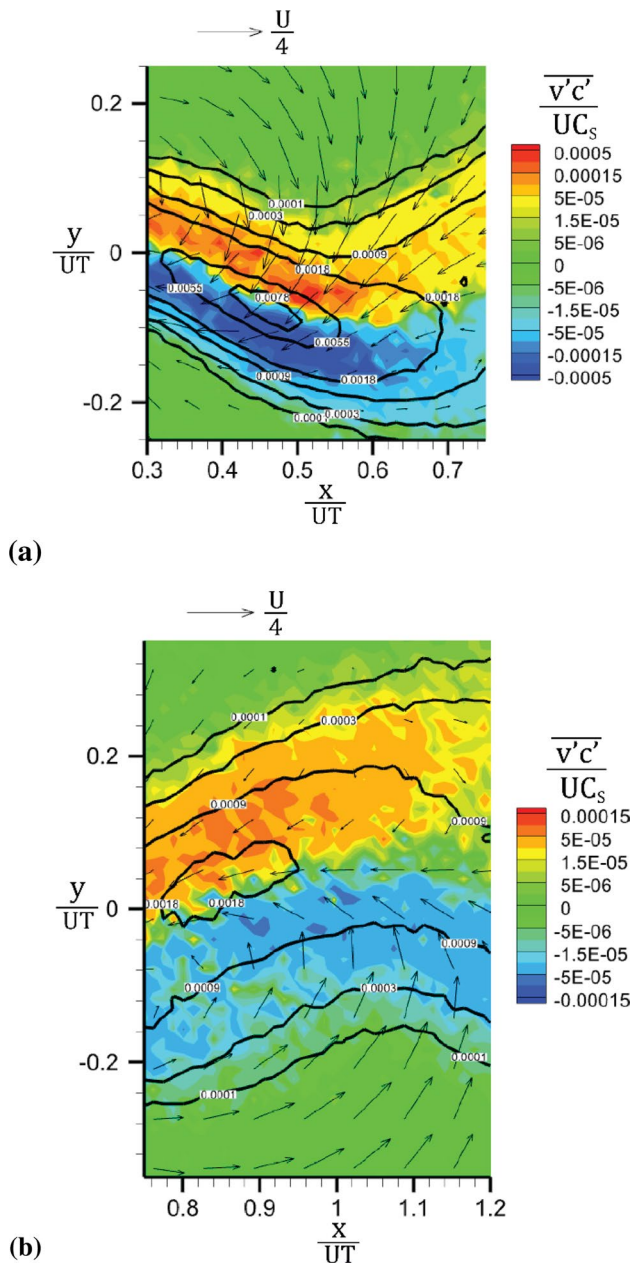


**Fig. 7** Turbulent flux in the  $y$ -direction ( $\overline{v'c'}/UC_s$ ) for the meandering plume for phase  $\varphi=0^\circ$  shown for the (a) zoom 1 and (b) zoom 2 regions defined in Fig. 6. Phase-averaged concentration iso-contour lines are shown in black (note they are logarithmically spaced). The vectors indicate the phase-averaged velocity with the free-stream velocity ( $U$ ) subtracted. Every 4th velocity vector is plotted

with the magnitude of the phase-averaged concentration gradient in the  $y$ -direction.

To confirm the efficacy of the eddy diffusivity model, it is necessary to directly examine the turbulent flux of scalar plotted as a function of phase-averaged concentration gradient. To accomplish this, phase-averaged concentration profiles were extracted at 20 downstream positions for each

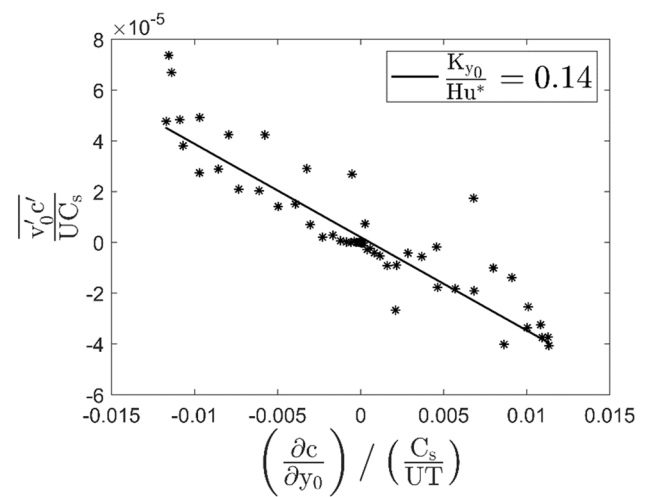


**Fig. 8** Turbulent flux of scalar ( $\overline{v'_0 c'}/UC_s$ ) in the direction perpendicular to the local plume centerline (i.e., along axis  $y_0$ ) as a function of the phase-averaged concentration gradient  $\left[\left(\frac{\partial c}{\partial y_0}\right) / \left(\frac{C_s}{UT}\right)\right]$  in the direction perpendicular to the local plume centerline at  $x/UT=0.95$  for phase  $\varphi=0^\circ$ . The slope of the line leads to the estimate of the eddy diffusivity coefficient  $\frac{K_{y0}}{Hu^*}$

of the four phases measured for the meandering plume, with the concentration profiles defined perpendicular to the local plume centerline (as in Young et al. 2021). This process aligns the axis of the analysis with the local gradient of the phase-averaged concentration (see Fig. 8 in Young et al. 2021) as well as the apparent orientation of the local gradient of the turbulent flux (see Figs. 5, 6 and 7). In subsequent analysis, the axis direction perpendicular to the local phase-averaged plume centerline is referred to as  $y_0$  (see Fig. 8 in Young et al. 2021).

The turbulent flux ( $\overline{v'_0 c'}$ ) along the concentration profile axis ( $y_0$ ) was calculated by defining  $16 \times 16$  pixel bins along the concentration profile axis and identifying the values of  $u'$ ,  $v'$ , and  $c'$  for each PTV vector in the bin. The PTV velocity vector components were rotated to align with the local plume centerline axis and the concentration profile axis to obtain  $u'_0$  (along-plume-centerline velocity fluctuation) and  $v'_0$  (cross-plume-centerline velocity fluctuation), respectively. The turbulent flux in the  $y_0$ -direction,  $\overline{v'_0 c'}$ , was calculated at the centroid of each bin along the concentration profile axis as the ensemble-average of  $v'_0 c'$  for every PTV vector located in each bin. The turbulent flux in the  $y_0$ -direction,  $\overline{v'_0 c'}$ , was plotted against the slope of the segmented Gaussian profile fit to the concentration profile (see Fig. 9 in Young et al. 2021) to ensure a smooth and continuous estimate of the phase-averaged concentration slope  $\left(\frac{\partial c}{\partial y_0}\right)$ .

An example plot of the turbulent flux along the concentration profile axis as a function of the phase-averaged concentration slope is shown in Fig. 8 for the meandering plume for



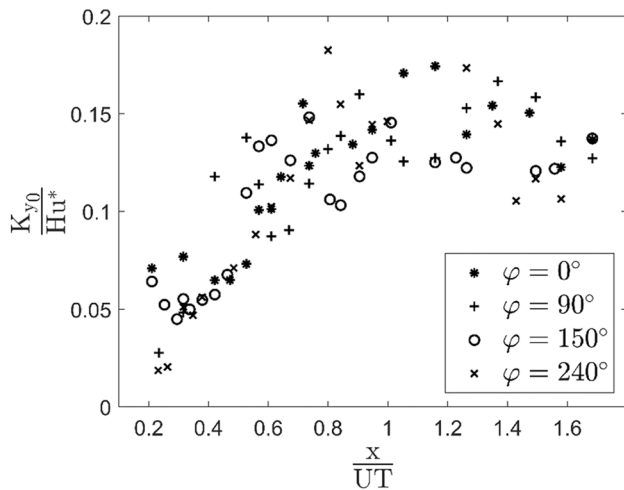
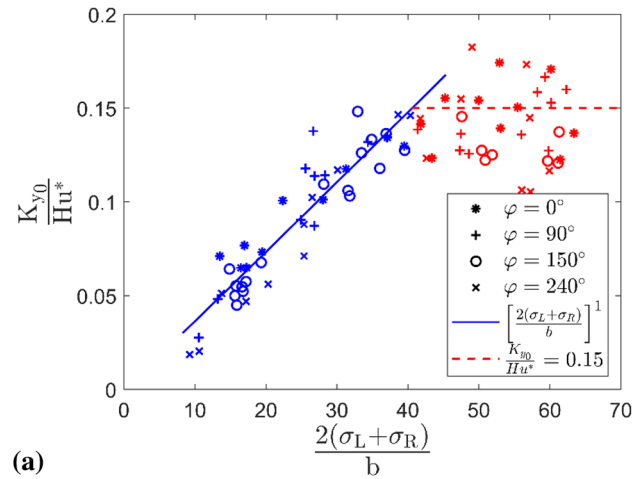


**Fig. 9** Eddy diffusivity coefficient ( $\frac{K_{y0}}{Hu^*}$ ) in the direction perpendicular to the local plume centerline (i.e., along axis  $y_0$ ) as a function of downstream distance ( $x/UT$ )

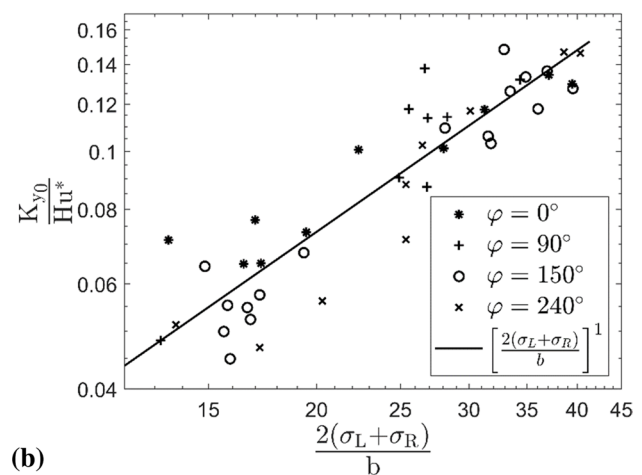
phase  $\varphi = 0^\circ$ . Figure 8 offers compelling evidence for a linear relationship between  $v'_{0c'}$  and  $\frac{\partial c}{\partial y_0}$  along the concentration profile with 82% of the variance in  $v'_{0c'}$  explained by the linear fit. The eddy diffusivity coefficient is calculated from this analysis as the slope of the linear fit and is reported with the standard non-dimensionalization using the water depth ( $H = 200$  mm) and the wall shear velocity ( $u^*$ ), measured to be 3.08 mm/s in the flume flow used in this experiment (see Fig. 2 in Young et al. 2021).

Figures 9 and 10 show the eddy diffusivity coefficient  $\frac{K_{y0}}{Hu^*}$  as a function of downstream distance and plume width, respectively. The eddy diffusivity coefficient increases with downstream distance until  $x/UT \cong 0.8$ , at which point it appears to level off. Figure 10a reveals the leveling-off of  $\frac{K_{y0}}{Hu^*}$  as a function of plume width. The continuous increase in the eddy diffusivity coefficient when the scalar patch is smaller than the integral length scale, followed by a leveling-off once the scalar patch exceeds integral length scale, is consistent with the foundational conceptualization that only turbulent eddies smaller than the scalar patch size contribute to turbulent mixing (e.g., Kundu et al. 2015). As the scalar patch becomes larger, larger and more energetic turbulent eddies are able to contribute to its mixing and the eddy diffusivity coefficient is expected to increase. Once the size of the scalar patch equals and exceeds the size of the largest turbulent eddies, larger eddies are not present to additionally contribute to turbulent mixing, and thus the eddy diffusivity coefficient is expected to plateau.

A ballpark estimate of the size of the largest eddies possible in open channel flow is the water depth  $H$ . For the flume in this study, the water depth is  $H/b = 48$  when non-dimensionalized by the diameter of the scalar-release nozzle,



**(a)**



**(b)**

**Fig. 10** Eddy diffusivity coefficient ( $\frac{K_{y0}}{Hu^*}$ ) in the direction perpendicular to the local plume centerline (i.e., along axis  $y_0$ ) as a function of the plume width  $\frac{2(\sigma_L + \sigma_R)}{b}$ . **a** Shown on linear axes, and **b** shown on log axes for the range for which the plume width is smaller than the size of the largest vortices

$b$ . Further, the current data facilitate a direct estimate of the large-scale alternating-sign vortices induced by the diverting plate. The size estimate of the large-scale alternating-sign vortices was made based on the vortices visible in the phase-averaged vorticity fields across all four phases by averaging the major and minor axis lengths. Non-dimensionalizing by the nozzle diameter ( $b$ ), the average size of the vortices under this criterion was 40.5—thus the vortices shed from the diverting plate are of similar size to the largest turbulent eddies expected to exist in this flow. Returning to Fig. 10a, note that  $\frac{K_{y0}}{Hu^*}$  begins to level off around  $\frac{2(\sigma_L + \sigma_R)}{b} \approx 40$  (the red symbols in Fig. 10a correspond to  $\frac{2(\sigma_L + \sigma_R)}{b} > 40$ ).

Using data from numerous sources, Fischer et al. (1979) estimated that the transverse eddy diffusivity coefficient in an open channel flow could be estimated by

$K_y \approx 0.15Hu^*$ . Other studies have reached a similar conclusion with slightly different coefficients (e.g.,  $K_y \approx 0.17Hu^*$  in Webel and Schatzmann 1984), but in nearly all cases the transverse eddy diffusivity coefficient was bounded by  $0.1Hu^* \leq K_y \leq 0.2Hu^*$ . In these studies,  $H$  is used to estimate the size of the largest turbulent eddies, and thus the transverse eddy diffusivity coefficient levels off at these values once the scalar patch has exceeded this size. The dashed red line in Fig. 10a represents  $\frac{K_{y0}}{Hu^*} = 0.15$  and agrees very well with the transverse eddy diffusivity coefficients estimated where the plume width exceeds the size of the largest eddies ( $\frac{2(\sigma_L + \sigma_R)}{b} > 40$ ).

Figure 10b addresses the growth of the eddy diffusivity coefficient before it reaches the size of the largest eddies. Figure 10b plots the eddy diffusivity coefficient as a function of plume width during the coefficient growth phase on a log–log scale with a least-square best-fit line shown. As described in Introduction, Richardson (1926) argued based on observations that  $K_y \propto L^{4/3}$ , where  $L$  is the characteristic size of the scalar patch. Later studies have corroborated this 4/3-power dependence, e.g., Stommel (1949), Brooks (1960), Foxworthy et al. (1966), and Okubo (1968). However, in a compilation of the results from many experiments, Okubo (1971) found that, although the 4/3-power relationship was followed locally within each experiment, when experiments were combined the eddy diffusivity coefficient scaled closer to  $K_y \propto L^{1.15}$ . To maintain generality, later studies (Stacey et al. 2000; Fong and Stacey 2003) have assumed that the eddy diffusivity coefficient can be estimated by  $K_y = \alpha L^n$ , allowing other values of  $n$  to be examined. Fong and Stacey (2003) provide a discussion of the idealized values of  $n=0, 1, 4/3$ , and 2 and fit their coastal plume data to predict  $n=1.5$ . Stacey et al. (2000) further argue that  $n$  may vary with downstream distance, specifically that it may be appropriate to employ  $n=4/3$  in the near field and  $n=0$  (i.e., constant diffusivity), when the plume scaling has exceeded the integral length scale, with intermediate values in the space between.

The eddy diffusivity coefficient observed for the meandering plume in this study scales with plume width to the power of  $n=1$ , i.e.,  $\left(\frac{2(\sigma_L + \sigma_R)}{b}\right)^1$  (Fig. 10b). Csanady (1973) and others provide a relationship between the plume width and the eddy diffusivity coefficient:  $K_y = \frac{U}{2} \frac{d\sigma^2}{dx}$ . This relationship is often used to estimate the eddy diffusivity coefficient based on measurements of the plume width. However, the relationship can be used here to confirm the power coefficient observed in Fig. 10b. The meandering plume width grows as  $x^1$  (see Fig. 10b in Young et al. 2021). Thus,

$$K_y = \frac{U}{2} \frac{d\sigma^2}{dx} \sim \frac{U}{2} \frac{dx^2}{dx} = Ux^1 \sim \left(\frac{2(\sigma_L + \sigma_R)}{b}\right)^1$$

This scaling relationship matches the trend in Fig. 10b, thereby demonstrating consistency. This trend is also generally consistent with the findings of Okubo (1971), Stacey et al. (2000), and Fong and Stacey (2003). Further, Brooks (1960) included the  $n=1$  case as one of his examples of varying turbulent diffusivity coefficient.

## 4 Conclusions

The large-scale alternating sign vortices strongly influence the spatial distribution of the turbulence quantities. Combining the phase-averaged concentration profiles in Young et al. (2021) with the turbulent flux presented in this study, the eddy diffusivity hypothesis successfully modeled the turbulent flux of scalar in the meandering plume. Hence, the conceptual idea to separate the meandering scales and turbulent scales when considering turbulent mixing in a meandering scalar plume appears valid for this plume. Unsurprisingly, the size of the plume relative to the largest eddies—which roughly match the size of the large-scale alternating sign vortices—dictates the behavior of the eddy diffusivity coefficient. When the plume width is larger than the size of the largest eddies, the eddy diffusivity coefficient is a constant, given by  $K_{y0} \approx 0.15Hu^*$ . This agrees well with other studies' estimates of the eddy diffusivity coefficient in open channel flows (e.g., Fischer et al. 1979; Webel and Schatzmann 1984). When the plume width is smaller than the size of the largest eddies, the eddy diffusivity coefficient scales as the plume width to the power of  $n=1$ .

The turbulent diffusivity results reported here may be incorporated into modeling efforts for naturally meandering plumes. The one-directional coupling between the velocity equations and scalar transport equations suggests the velocity field may be specified or simulated separately for calculation of the advection–diffusion equation (Eq. 2) combined with the eddy diffusivity model (Eq. 3). The challenges of this approach include managing the separation of time-scales between the large-scale oscillating motion of the meandering and the modeled turbulent mixing. The alignment of the transverse turbulent diffusivity may require some iteration at each time-step. Further, turbulent diffusivity in the other coordinate directions will need to be incorporated into the simulation as well.

**Acknowledgments** The authors thank Dr. Phil Roberts (Georgia Institute of Technology) for helpful discussions.

**Funding** The authors gratefully acknowledge financial support provided by the University of Gothenburg, the Swedish Research Council FORMAS (Dnr: 2012–1134), and the US National Science Foundation via grant OCE-1234449.

## References

- Arcoumanis C, McQuirk JJ, Palma JMLM (1990) On the use of fluorescent dyes for concentration measurements in water flows. *Exp Fluids* 10:177–180. <https://doi.org/10.1007/BF00215028>
- Batchelor GK (1952) Diffusion in a field of homogeneous turbulence. II. The relative motion of particles. *Proc Camb Philos Soc* 48:345–362. <https://doi.org/10.1017/S0305004100027687>
- Brooks NH (1960) Diffusion of sewage effluent in an ocean-current. In: *Proceedings of 1st International conference on waste disposal in the marine environment*, University of California, pp. 246–267.
- Cowen EA, Chang K-A, Liao Q (2001) A single-camera coupled PTV-LIF technique. *Exp Fluids* 31:63–73. <https://doi.org/10.1007/s003480000259>
- Cowen EA, Monismith SG (1997) A hybrid digital particle tracking velocimetry technique. *Exp Fluids* 22:199–211. <https://doi.org/10.1007/s003480050038>
- Csanady GT (1973) *Turbulent diffusion in the environment*. D. Reidel Publishing Co., Boston
- Fischer HB, List EJ, Koh RCY, Imberger J, Brooks NH (1979) *Mixing in inland and coastal waters*. Academic Press, New York
- Fong DA, Stacey MT (2003) Horizontal dispersion of a near-bed coastal plume. *J Fluid Mech* 489:239–267. <https://doi.org/10.1017/S002211200300510X>
- Foxworthy JE, Tibby RB, Barsom GM (1966) Dispersion of a surface waste field in the sea. *J Water Pollut Control Feder* 38:1170–1193
- Gifford F (1959) Statistical properties of a fluctuating plume dispersion model. *Adv Geophys* 6:117–136. [https://doi.org/10.1016/S0065-2687\(08\)60099-0](https://doi.org/10.1016/S0065-2687(08)60099-0)
- Hanna SR (1986) Spectra of concentration fluctuations: the two time scales of a meandering plume. *Atmos Environ* 20:1131–1137. [https://doi.org/10.1016/0004-6981\(86\)90145-9](https://doi.org/10.1016/0004-6981(86)90145-9)
- Huang Z, Kawall JG, Keffer JF, Ferre JA (1995) On the entrainment process in plane turbulent wakes. *Phys Fluids* 7:1130–1141. <https://doi.org/10.1063/1.868554>
- Jeong J, Hussain F (1995) On the identification of a vortex. *J Fluid Mech* 285:69–94. <https://doi.org/10.1017/S0022112095000462>
- Jones NL, Lowe RJ, Pawlak G, Fong DA, Monismith SG (2008) Plume dispersion on a fringing coral reef system. *Limnol Oceanogr* 53:2273–2286. [https://doi.org/10.4319/lo.2008.53.5\\_part\\_2.2273](https://doi.org/10.4319/lo.2008.53.5_part_2.2273)
- Kim W, Yoo JY, Sung J (2006) Dynamics of vortex lock-on in a perturbed cylinder wake. *Phys Fluids* 18:074103. <https://doi.org/10.1063/1.2221350>
- Kolmogorov AN (1941) The local structure of turbulence in incompressible viscous fluid for very large Reynolds numbers. *Doklady Akademii Nauk SSSR* 30:301–305
- Kundu PK, Cohen IM, Dowling DR (2015) *Fluid mechanics*, 6th edn. Elsevier Academic Press, Cambridge MA
- Liao Q, Cowen EA (2010) Relative dispersion of a scalar plume in a turbulent boundary layer. *J Fluid Mech* 661:412–445. <https://doi.org/10.1017/S0022112010003058>
- Lyn DA, Einav S, Rodi W, Park JH (1995) A laser-Doppler velocimetry study of the ensemble-averaged characteristics of the turbulent near wake of a square cylinder. *J Fluid Mech* 304:285–319. <https://doi.org/10.1017/S0022112095004435>
- Maas HG, Gruen A, Papantoniou D (1993) Particle tracking velocimetry in three-dimensional flows. Part 1. Photogrammetric determination of particle coordinates. *Exp Fluids* 15:133–146. <https://doi.org/10.1007/BF00190953>
- Malik NA, Dracos T, Papantoniou DA (1993) Particle tracking velocimetry in three-dimensional flows. Part 2. Particle tracking. *Exp Fluids* 15:279–294. <https://doi.org/10.1007/BF00223406>
- Nakagawa S, Nitta K, Senda M (1999) An experimental study on unsteady turbulent near wake of a rectangular cylinder in channel flow. *Exp Fluids* 27:284–294. <https://doi.org/10.1007/s003480050353>
- Okubo A (1968) Some remarks on the importance of the “shear effect” on horizontal diffusion. *J Oceanogr Soc Jpn* 24:60–69
- Okubo A (1971) Oceanic diffusion diagrams. *Deep-Sea Res* 18:789–802. [https://doi.org/10.1016/0011-7471\(71\)90046-5](https://doi.org/10.1016/0011-7471(71)90046-5)
- Pope SB (2000) *Turbulent flows*. Cambridge University Press, Cambridge
- Rahman S, Webster DR (2005) The effect of bed roughness on scalar fluctuations in turbulent boundary layers. *Exp Fluids* 38:372–384. <https://doi.org/10.1007/s00348-004-0919-7>
- Richardson LF (1926) Atmospheric diffusion shown on a distance-neighbour graph. *Proc Royal Soc London A* 110:709–737. <https://doi.org/10.1098/rspa.1926.0043>
- Roberts PJ, Webster DR (2002) Turbulent diffusion. In: Shen HH, Cheng AHD, Wang K, Teng MH, Liu CCK (eds) *Environmental fluid mechanics: theories and applications*. American Society of Civil Engineers, Reston, VA, pp 7–47 DOI:<https://doi.org/10.1002/9780470057339.vat029>
- Saha AK, Muralidhar K, Biswas G (2000) Vortex structures and kinetic energy budget in two-dimensional flow past a square cylinder. *Comput Fluids* 29:669–694. [https://doi.org/10.1016/S0045-7930\(99\)00021-3](https://doi.org/10.1016/S0045-7930(99)00021-3)
- Sawford BL, Stapountzis H (1986) Concentration fluctuations according to fluctuating plume models in one and two dimensions. *Bound-Layer Meteorol* 37:89–105. <https://doi.org/10.1007/BF00122758>
- Stacey MT, Cowen EA, Powell TM, Dobbins E, Monismith SG, Kosseff JR (2000) Plume dispersion in a stratified near-coastal flow: measurements and modeling. *Cont Shelf Res* 20:637–663. [https://doi.org/10.1016/S0278-4343\(99\)00061-8](https://doi.org/10.1016/S0278-4343(99)00061-8)
- Stommel H (1949) Horizontal diffusion due to oceanic turbulence. *J Mar Res* 8:199–225
- Talluru KM, Philip J, Chauhan KA (2018) Local transport of passive scalar released from a point source in a turbulent boundary layer. *J Fluid Mech* 846:292–317. <https://doi.org/10.1017/jfm.2018.280>
- Tracy HJ, Lester CM (1961) Resistance coefficients and velocity distribution smooth rectangular channel. US Geological Survey Water Supply Paper 1592-A DOI: <https://doi.org/10.3133/wsp1592A>
- Vanderwel C, Tavoularis S (2014) Measurements of turbulent diffusion in uniformly sheared flow. *J Fluid Mech* 754:488–514. <https://doi.org/10.1017/jfm.2014.406>
- Webel G, Schatzmann M (1984) Transverse mixing in open channel flow. *J Hydraul Eng* 110:423–435. [https://doi.org/10.1061/\(ASCE\)0733-9429\(1984\)110:4\(423\)](https://doi.org/10.1061/(ASCE)0733-9429(1984)110:4(423))
- Webster DR, Rahman S, Dasi LP (2003) Laser-induced fluorescence measurements of a turbulent plume. *J Eng Mech* 129:1130–1137. [https://doi.org/10.1061/\(ASCE\)0733-9399\(2003\)129:10\(1130\)](https://doi.org/10.1061/(ASCE)0733-9399(2003)129:10(1130))
- Webster DR, Roberts PJW, Ra’ad L (2001) Simultaneous DPTV/PLIF measurements of a turbulent jet. *Exp Fluids* 30:65–72. <https://doi.org/10.1007/s003480000137>
- Young DL, Larsson AI, Webster DR (2021) Structure and mixing of a meandering turbulent chemical plume: concentration and velocity fields. *Exp Fluids* 62:240. <https://doi.org/10.1007/s00348-021-03337-x>

**Publisher's Note** Springer Nature remains neutral with regard to jurisdictional claims in published maps and institutional affiliations.